ORIGINAL ARTICLE

lajss.org© Latin American Journal of Solids and Structures

www.lajss.org

Elastoplastic Analysis of Perforated Metal Sheets using Transformation Field Analysis and Finite Element Method

Christiano Augusto Ferrário Várady Filho[a]*, Márcio André Araújo Cavalcante[b]

[a] Centro de Tecnologia, Universidade Federal de Alagoas, Maceió, Brasil. Email: christiano_varady@lccv.ufal.br

[b] Campus de Engenharias e Ciências Agrárias, Universidade Federal de Alagoas, Rio Largo, Brasil. Email: marcio.cavalcante@ceca.ufal.br

* Corresponding author

https://doi.org/10.1590/1679-78256650

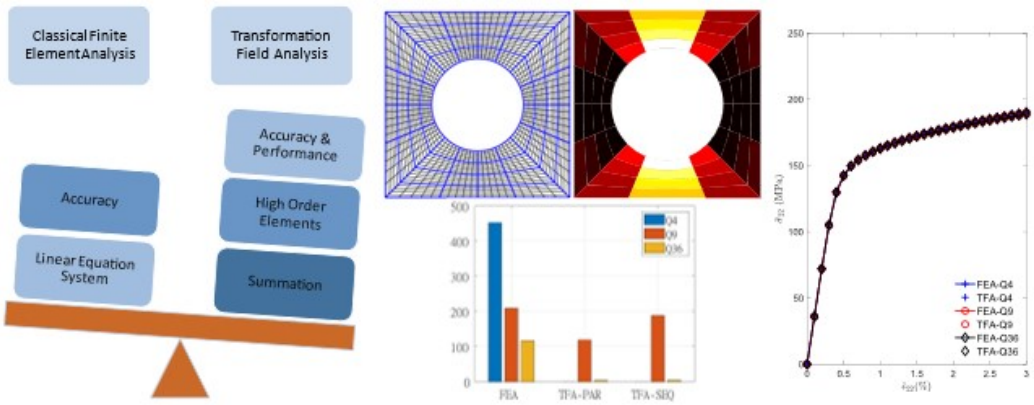
Abstract

This investigation analyzes the cost-benefit ratio of the Transformation Field Analysis to compute the elastoplastic behavior of periodically perforated metal sheets. Evaluation of accuracy and computational cost are analyzed by implementing a finite element approach coupled with the Transformation Field Analysis technique for different meshes and finite element orders. Numerical studies are employed to compare Transformation Field Analysis accuracy with standard Finite Element Analysis for elastoplastic analysis of periodically perforated metal sheets. Additionally, experimental data is employed to validate the Transformation Field Analysis results. The Transformation Field Analysis requires calculating the strain concentration and influencing tensors employing the finite element method. The numerical results show the technique's capabilities and favorable scenarios, besides the influence of domain discretization and finite element order.

Keywords

Transformation Field Analysis, Perforated Metal Sheets, Finite Element Method, High Order Elements, and Computational Performance.

Graphical Abstract



Received July 11, 2021. In revised form July 23, 2021. Accepted July 23, 2021. Available online July 27, 2021.
https://doi.org/10.1590/1679-78256650

Latin American Journal of Solids and Structures. ISSN 1679-7825. Copyright © 2021. This is an Open Access article distributed under the terms of the Creative Commons Attribution License, which permits unrestricted use, distribution, and reproduction in any medium, provided the original work is properly cited.

1 INTRODUCTION

Micromechanics of porous materials assesses the influence of the porous's geometrical configuration and mechanical properties of the matrix material by homogenization and multiscale techniques. Determination of the homogenized inelastic response of porous materials integrated into a multiscale analysis continues to challenge researchers because of the complex microstructure stress and inelastic strain fields.

An example is the Generalized Cell Method (GMC) created by Paley and Aboudi (1992) and reformulated by Pindera and Bednarcyk (1999). The GMC models complex periodic unit cells and allows the coupling of different constitutive laws to evaluate the local response of materials. Another approach for homogenization of composite materials is the Locally Exact Homogenization Theory (LEHT) proposed by Drago and Pindera (2008), which evaluates effective parameters of periodic materials using locally applied elastic solutions. The method was first employed in periodic composite materials reinforced along one direction by isotropic cylindrical fibers distributed in a squared array, Figure 1(a). Later, Wang and Pindera (2016) expanded to the parametrical analysis of orthotropic and transversally isotropic materials with a hexagonal array, Figure 1(b). Recently, the Generalized Finite-Volume Direct Averaging Micromechanics (GFVDAM), as presented in Cavalcante and Pindera (2016), uses a higher-order displacement field to achieve kinematic conformity and stress/strain fields continuity among all subdomains of the discretized analyzed domain.

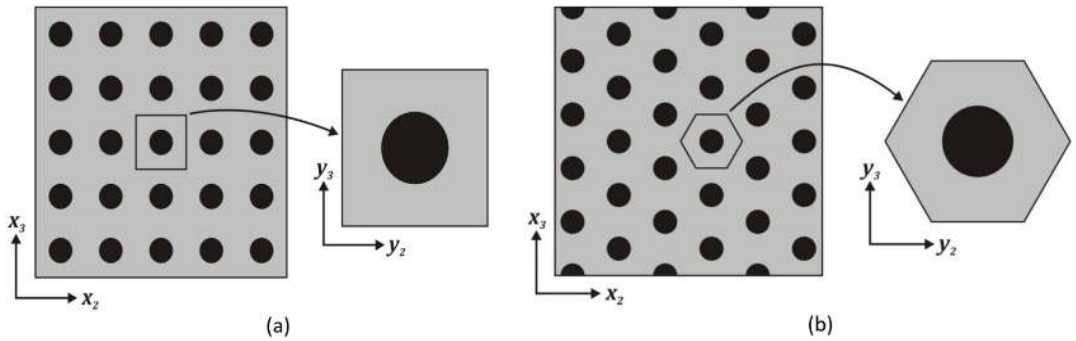


Figure 1: Squared (a) and hexagonal (b) arrays.

Those techniques are alternatives to the Finite Element Method (FEM) for mechanical analysis of periodic media. The increase in sophistication of the models and evaluation of localized phenomena requires refined discretized domains or higher-order finite elements. Some techniques address the classical Finite Element Analysis (FEA) to enhance performance. The Transformation Field Analysis (TFA) is one of them, Dvorak (1986). The TFA solves the non-linear analysis by adding fundamental solutions based on the concepts of concentration and influence tensors borrowed from the micromechanics analysis and applying the superposition principle.

The TFA is a procedure that decomposes the elastic strain field in a superposition of uniform eigenstrain fields, exploiting the dependence of the subdomains displacement fields and its influence in the global field, Dvorak (1986). The TFA relates thermal and mechanical loadings even when the phases' properties depend on the temperature variation, Benveniste and Dvorak (1990). In the TFA approach, Dvorak proposes reducing the number of calculated variables, optimizing the cost-benefit ratio of the simulation.

The superposition-based formulation can also be found in Dvorak (1990), where uniform fields in a biphasic medium can be assessed. In this work, the authors calculate the influence tensors based on unit eigenstrains and define their relations with inelastic strains, considering an arbitrary geometry for the phases. They also restrict the type of inclusions where uniform strain fields are available. Additionally, Benveniste and Dvorak (1992) makes some observations of the uniform field in composite materials. In the same year, Dvorak and Benveniste (1992) expanded Dvorak's formulation for multi-phase composites, and a FEM-based approach for TFA is proposed in Dvorak et al. (1994), wherein the first comparison of classic FEA and TFA is investigated, and TFA shows good accuracy.

Following publications complemented the developments and applications of the TFA formulation. Michel and Suquet (2003) proposed a methodology using non-uniform fields (Non-Uniform Transformation Field Analysis - NTFA). This modification reduced the number of microscale subdivisions necessary to evaluate the composite material's effective constitutive relationships accurately. An application was presented in Michel and Suquet (2004) for an aluminum sheet with Boron fibers subjected to macroscopic stresses, and the differences between the TFA and NTFA formulations were evaluated for the same meshes. Additionally, Roussette et al. (2009) applied NTFA and the Karhunen-Loève decomposition for porous and composite materials considering a viscoelastoplastic regime.

Developments of the NTFA are presented in Fritzen and Leuschner (2013) and Sepe et al. (2013). The first adopts a variational approach to solve the reduction problem in the plastic regime, and the second differs from NTFA by using linear combinations of inelastic fields for each element and testing its procedure in shape memory alloys (SMA). A comparison between the two methods is presented in Fritzen et al. (2015), discerning situations where each method stands out. Addessi et al. (2010) adapt TFA for numerical analysis of masonry, and Cavalcante and Pindera (2013) proposed a TFA approach based on the Finite-Volume Direct Averaging Micromechanics (FVDAM) theory.

Recently, Covezzi et al. (2017) proposed a modification to the method, where instead of approximating the inelastic strain field, the approximation of a stress field is considered. Covezzi et al. (2018) complemented the comparison previously made in Fritzen et al. (2015), introducing this new technique. In this regard, Yang et al. (2020) proposed a homogenization technique with second-order reduced factors based on TFA and applied it in axisymmetric configurations.

An exciting optimization technique is presented in Alaimo et al. (2019), where decomposition of the strain field based on the Principal Component Analysis (PCA) technique is employed to identify regions of the analyzed domain where it is more interesting to apply TFA or employ standard FEA. This technique was applied in a unit cell model considering a viscoelastic constitutive regime.

It is essential to point out two significant challenges in the application of TFA: the approximation of the inelastic field (the bases that are employed for its calculation) and the accurate solution of the temporal evolution problem of the inelastic field, which is related to the number of variables calculated step by step along the time. Several applications are addressing both problems, but their resolutions are still challenging.

This investigation addresses the second challenge, analyzing the performance of the TFA-based Finite Element approach for elastoplastic analysis of periodic porous media. Evaluation of numerical and experimental case studies appraise accuracy and computational cost for different discretizations, considering h- and p- refinements in FEA to assess favorable scenarios for applying the technique.

2 HOMOGENIZATION OF PERIODIC MATERIALS

Mechanical analysis of periodic materials under homogeneous loading is defined by the behavior of the repeating unit cell, which consists of the pattern used to generate the whole material. The solution of the boundary-value problem subject to periodic traction and displacement boundary conditions defines the macroscale response of the material (Drago and Pindera, 2007).

The unit cell should be well enough discretized to capture the microstructural details. Also, the displacement field in subdomains is expressed in terms of macroscopic and local contributions using a two-scale expansion in global and local coordinates,

$$u_i^{(q)}(\boldsymbol{x},\boldsymbol{y}) = \overline{\varepsilon}_{ij}x_j + \tilde{u}_i^{r(q)}(\boldsymbol{y})\,, i = 1,2,3 \tag{1}$$

where $\overline{\varepsilon}_{ij}$ is the macroscopic strain field applied to the entire material and $\tilde{u}_i^{r(q)}(\boldsymbol{y})$ is the local fluctuating displacement in the qth subdomain for the rth phase. Accordingly, the strain field is also decomposed into average and fluctuating parts $\varepsilon_i^{(q)}(\boldsymbol{x},\boldsymbol{y}) = \overline{\varepsilon}_{ij} + \tilde{\varepsilon}_{ij}^{r(q)}(\boldsymbol{y})$. FEA solution produces a set of equations for the parameters defining the subdomain fluctuating displacement field of the form

$$\boldsymbol{K}\tilde{\boldsymbol{u}} = \Delta\boldsymbol{C}\overline{\boldsymbol{\varepsilon}} + \boldsymbol{G}\left(\int_{V(q)} \boldsymbol{\varepsilon}^{p(q)} dV\right) \tag{2}$$

with $\Delta\boldsymbol{C}$ having terms of the differences in the stiffness matrix, $\boldsymbol{G}$ contains volume integrals of the unknown plastic strains over the subdomains and $\tilde{\boldsymbol{u}}$ represent nodal fluctuating displacements that are common to adjacent subdomains, which depends only on the plastic strain field $\boldsymbol{\varepsilon}^{p(q)}$.

Solution of the system, coupled with homogeneous displacement field, determines the displacement in each subdomain, wherein the volume-averaged strain in the qth subdomain can be evaluated as

$$\overline{\boldsymbol{\varepsilon}}^{(q)} = \boldsymbol{A}^{(q)}\overline{\boldsymbol{\varepsilon}} + \boldsymbol{D}^{(q)} \tag{3}$$

with $\boldsymbol{A}^{(q)}$ and $\boldsymbol{D}^{(q)}$ as the elastic strain concentration tensors (Hill, 1963) and inelastic influence tensors, respectively. Based on these definitions, using subdomain stresses and strains through local constitutive equations

$$\boldsymbol{\sigma}^{(q)} = \boldsymbol{C}^{(q)}\left(\boldsymbol{\varepsilon}^{(q)} - \boldsymbol{\varepsilon}^{p(q)}\right) \tag{4}$$

we can evaluate the volume-averaged stress in terms of the volume-averaged subdomain stress

$$\overline{\boldsymbol{\sigma}} = \frac{1}{V}\sum_{q=1}^{N_q}\int_{V_q}\boldsymbol{\sigma}^{(q)}dV = \sum_{q=1}^{N_q} c_{(q)}\overline{\boldsymbol{\sigma}}^{(q)} = \sum_{q=1}^{N_q} c_{(q)}\boldsymbol{C}^{(q)}\left(\overline{\boldsymbol{\varepsilon}}^{(q)} - \overline{\boldsymbol{\varepsilon}}^{p(q)}\right) = \boldsymbol{C}^{*}\left(\overline{\boldsymbol{\varepsilon}} - \overline{\boldsymbol{\varepsilon}}^{p}\right) \tag{5}$$

which is the homogenized Hooke's law. The homogenized stifness matrix $\boldsymbol{C}^{*}$ and plastic strain $\overline{\boldsymbol{\varepsilon}}^{p(q)}$ can be evaluated as

$$\boldsymbol{C}^{*} = \sum_{q=1}^{N_q} c_{(q)}\boldsymbol{C}^{(q)}\boldsymbol{A}^{(q)}, \tag{6}$$

$$\overline{\boldsymbol{\varepsilon}}^{p} = [\boldsymbol{C}^{*}]^{-\mathbf{1}}\sum_{q=1}^{N_q} c_{(q)}\boldsymbol{C}^{(q)}\left(\overline{\boldsymbol{\varepsilon}}^{p(q)} - \boldsymbol{D}^{(q)}\right) \tag{7}$$

where $\overline{\boldsymbol{\varepsilon}}^{p(q)}$ is the volume-averaged plastic strains in the qth subdomain. Calculation of the strain concentration and influence tensors is presented in next section.

2.1 Transformation Field Analysis

Eigenstrains, from which TFA is based, is a mathematical concept and can represent some physical phenomenon in the manufacture or operation of composite materials caused by thermal changes, variations in the humidity of the phase material, or inelastic strains. It is essential to point out that the strains caused by stresses superior to the material's yield stress can be decomposed into its elastic and inelastic parts, and only the latter is an eigenstrain. Also, for an incremental increase in the stress field, changes in the inelastic strain field depend on the loading history.

The presence of eigenstrain $\boldsymbol{\mu}^{(r)}$ and eigenstress $\boldsymbol{\lambda}^{(r)}$ in the rth phase affects the constitutive relationships as follows

$$\boldsymbol{\sigma}^{(r)} = \boldsymbol{C}^{(r)}\boldsymbol{\varepsilon}^{(r)} + \boldsymbol{\lambda}^{(r)} \leftrightarrow \boldsymbol{\varepsilon}^{(r)} = \boldsymbol{S}^{(r)}\boldsymbol{\sigma}^{(r)} + \boldsymbol{\mu}^{(r)} \text{ where} \tag{8}$$

$$\boldsymbol{\lambda}^{(r)} = -\boldsymbol{C}^{(r)}\boldsymbol{\mu}^{(r)} \text{ and } \boldsymbol{\mu}^{(r)} = -\boldsymbol{S}^{(r)}\boldsymbol{\lambda}^{(r)} \tag{9}$$

$$\therefore \boldsymbol{\sigma}^{(r)} = \boldsymbol{C}^{(r)}\left[\boldsymbol{\varepsilon}^{(r)} - \boldsymbol{\mu}^{(r)}\right] \leftrightarrow \boldsymbol{\varepsilon}^{(r)} = \boldsymbol{S}^{(r)}\left[\boldsymbol{\sigma}^{(r)} - \boldsymbol{\lambda}^{(r)}\right]. \tag{10}$$

An interesting way of representing the local stress/strain fields in a heterogeneous media is to employ transformation variables with uniform distributions, as proposed in Dvorak (1990). Thus, the volume-averaged strain and stress in the rth phase can be evaluated as follows

$$\overline{\boldsymbol{\varepsilon}}^{(r)} = \boldsymbol{A}^{(r)}\overline{\boldsymbol{\varepsilon}} + \sum_{s=1}^{N}\boldsymbol{D}^{(r,s)}\overline{\boldsymbol{\mu}}^{(s)} \text{ and } \overline{\sigma}^{(r)} = \boldsymbol{B}^{(r)}\overline{\boldsymbol{\sigma}} + \sum_{s=1}^{N}\boldsymbol{F}^{(r,s)}\overline{\boldsymbol{\lambda}}^{(s)} \tag{11}$$

where $\boldsymbol{A}^{(r)}$ and $\boldsymbol{B}^{(r)}$ are the strain and stress concentration tensors for the rth phase, respectively. The tensors $\boldsymbol{D}^{(r,s)}$ and $\boldsymbol{F}^{(r,s)}$ are called transformation influence tensors for strain and stress, respectively. They measure the strain/stress in the rth phase caused by uniform eigenfields $\overline{\boldsymbol{\mu}}^{(s)}$ and $\overline{\boldsymbol{\lambda}}^{(s)}$ in the sth phase applied in a model where $\overline{\boldsymbol{\varepsilon}} = \mathbf{0}$ and $\overline{\boldsymbol{\sigma}} = \mathbf{0}$, respectively. The influence tensors $\boldsymbol{D}^{(r,r)}$ and $\boldsymbol{F}^{(r,r)}$ indicate self-induced influences in the analysis. In biphasic materials (matrix and inclusions of the same type of material), the influence tensors can be calculated as

$$\boldsymbol{D}^{(r,m)} = \left(\boldsymbol{I} - \boldsymbol{A}^{(r)}\right)\left(\boldsymbol{C}^{(m)} - \boldsymbol{C}^{(i)}\right)^{-1}\boldsymbol{C}^{(m)}\ \boldsymbol{F}^{(r,m)} = \left(\boldsymbol{I} - \boldsymbol{B}^{(r)}\right)\left(\boldsymbol{S}^{(m)} - \boldsymbol{S}^{(i)}\right)^{-1}\boldsymbol{S}^{(m)} \tag{12}$$

$$\boldsymbol{D}^{(r,i)} = -\left(\boldsymbol{I} - \boldsymbol{A}^{(r)}\right)\left(\boldsymbol{C}^{(m)} - \boldsymbol{C}^{(i)}\right)^{-1}\boldsymbol{C}^{(i)}\ \boldsymbol{F}^{(r,i)} = -\left(\boldsymbol{I} - \boldsymbol{B}^{(r)}\right)\left(\boldsymbol{S}^{(m)} - \boldsymbol{S}^{(i)}\right)^{-1}\boldsymbol{S}^{(i)} \tag{13}$$

for $r = m, i$.

Transformational influence tensors have emerged as an alternative for evaluating inelastic behavior caused by different types of loads. Coupling with Finite Element Analysis (displacement formulation) involves the evaluation of

strain concentration and influence tensors for each finite element. The main advantage is that these tensors are evaluated just once, allowing for inelastic analysis in various situations (different loadings).

Calculation of Strain Concentration Tensors

Strain concentration tensors are evaluated in turns, where each shift fills the values of parts of the tensor. Each shift consists of the solution of the model with the application of components of macroscopic stress and strain ($\overline{\boldsymbol{\varepsilon}}_k = \boldsymbol{i}_k$ or $\overline{\boldsymbol{\sigma}}_k = \boldsymbol{i}_k$), where $\boldsymbol{i}_k$ is the kth column of the identity tensor. For each calculated solution, the volume-averaged local strains compose the columns of the strain concentration tensors. Below, the representation of a pseudo-algorithm for the calculation of the strain concentration tensors.

For each macroscopic strain $\overline{\boldsymbol{\varepsilon}}_k$:

1. Calculate the global force vector for the macroscopic strain $\overline{\boldsymbol{\varepsilon}}_k$;
2. Calculate the global fluctuating displacement vector $\widetilde{\boldsymbol{u}}$;
3. For each element e: the column related to component k is the sum of the macroscopic homogenous strain and the volume-averaged fluctuating strain of each finite element, which is obtained by multiplying the volume-averaged strain tensor $\overline{\boldsymbol{B}}^{(e)}$ and the local fluctuating displacement vector $\widetilde{\boldsymbol{u}}^{(e)}$:

$$\boldsymbol{A}^{(e)}(k,:) = \overline{\boldsymbol{\varepsilon}} + \overline{\boldsymbol{B}}^{(e)}\widetilde{\boldsymbol{u}}^{(e)} \tag{14}$$

Calculation of Transformation Influence Tensors

The process for evaluation of the influence tensors is similar. Macroscopic strain (or stress) tensors ($\overline{\boldsymbol{\varepsilon}} = \boldsymbol{0}$ or $\overline{\boldsymbol{\sigma}} = \boldsymbol{0}$) are applied. Next, the model is submitted to unit values for each eigenstrain component $\overline{\boldsymbol{\mu}}_k^{(\hat{e})} = \boldsymbol{i}_k$ in the element $\hat{e}$. For each component applied, the volume-averaged strain is calculated for all elements, composing each column of the influence tensor $\boldsymbol{D}^{(e,\hat{e})}$ in the element $\hat{e}$. Below, the representation of a pseudo-algorithm for the calculation of the transformation influence tensors.

For each eigenstrain $\overline{\boldsymbol{\mu}}_k^{(\hat{e})} = \boldsymbol{i}_k$:

1. Calculate the global force vector for the local eigenstrain $\overline{\boldsymbol{\mu}}_k^{(\hat{e})}$ in the element $\hat{e}$.
2. Calculate the global fluctuating displacement vector $\widetilde{\boldsymbol{u}}$;
3. For each element e: the column related to the k component of the influence tensor is the product between the volume-averaged strain tensor $\overline{\boldsymbol{B}}^{(e)}$ and the local fluctuating displacement vector $\widetilde{\boldsymbol{u}}^{(e)}$:

$$\boldsymbol{D}^{(e,\hat{e})}(k,:) = \overline{\boldsymbol{B}}^{(e)}\widetilde{\boldsymbol{u}}^{(e)} \tag{15}$$

2.2 Elastoplastic Analysis

Evaluation of the elastic strain concentration and plastic influence tensors permits calculation of the homogenized elastic-plastic behavior of a periodic material for all loading steps. Assessment of the mechanical behavior is done by successive integrations in incremental form of the homogenized plastic strains using the localization equations. The homogenized plastic strain increment is given as

$$d\overline{\boldsymbol{\varepsilon}}^{p} = \sum_{e=1}^{N_e} c_{(e)}\boldsymbol{B}^{(e)}d\overline{\boldsymbol{\varepsilon}}^{p(e)} \tag{16}$$

where the elastic stress concentration tensor is evaluated by $\boldsymbol{B}^{(e)} = [\boldsymbol{C}^{*}]^{-1}\left[\boldsymbol{A}^{(e)}\right]^{T}\boldsymbol{C}^{(e)}$ and the local plastic strain increment $d\overline{\boldsymbol{\varepsilon}}^{p(e)}$ is determined by plasticity theory with isotropic hardening employing Mendelson's reformulation of the Prandtl-Reuss Equations in terms of the strain deviators e'_{ij} (Mendelson, 1968)

$$d\overline{\varepsilon}_{ij}^{p(e)} = \left(\frac{\overline{e}_{ij}{}'}{\overline{e}_{eff}}\right)^{(e)} d\overline{\varepsilon}_{eff}^{p(e)} \text{ where} \tag{17}$$

$$\overline{e}_{eff} = \sqrt{\frac{2}{3}\bar{e}'_{ij}\bar{e}'_{ij}} \text{ and} \tag{18}$$

$$\bar{e}'_{ij} = \bar{\varepsilon}_{ij} - \frac{1}{3\bar{\varepsilon}_{kk}}\delta_{ij} - \bar{\varepsilon}^{p}_{ij}|_{previous} \tag{19}$$

with $\bar{\varepsilon}^{p}_{ij}|_{previous}$ being the plastic strains of the previous load step. The effective plastic strain increment is

$$d\overline{\varepsilon}^{p(e)}_{eff} = \overline{e}^{(e)}_{eff} - \overline{\sigma}^{(e)}_{eff}/3\mu \tag{20}$$

where $\overline{\sigma}^{(e)}_{eff}$ is the effective von-Mises stress in the element e. The load history is defined by homogenized strain increment $d\overline{\boldsymbol{\varepsilon}}$, and the subdomain plastic strains are calculated iteratively using the method of successive elastic solutions proposed in Mendelson (1968), decomposing uniform subdomain plastic strains in previous and incremental parts

$$\bar{\varepsilon}^{p(e)}_{ij} = \bar{\varepsilon}^{p(e)}_{ij}|_{previous} + d\bar{\varepsilon}^{p(e)}_{ij} \tag{21}$$

A pseudo-algorithm is presented below for each loading step:

1. Definition of the homogenized strain increment $d\overline{\boldsymbol{\varepsilon}}$;
2. Evaluation of the volume-averaged total strain in every element e:
   a. Apply the localization relation $\overline{\boldsymbol{\varepsilon}}^{(e)} = \boldsymbol{A}^{(e)}\overline{\boldsymbol{\varepsilon}} + \sum_{r=1}^{N_e}\boldsymbol{D}^{(e,\hat{e})}\overline{\boldsymbol{\varepsilon}}^{p(\hat{e})}$ (initially, $\bar{\varepsilon}^{p(\hat{e})}_{ij} = \bar{\varepsilon}^{p(\hat{e})}_{ij}|_{previous}$);
   b. Calculate $d\overline{\varepsilon}^{p(e)}_{ij} = \left(\frac{\bar{e}'_{ij}}{\overline{e}_{eff}}\right)^{(e)} d\overline{\varepsilon}^{p(e)}_{eff}$;
   c. Find $\bar{\varepsilon}^{p(e)}_{ij} = \bar{\varepsilon}^{p(e)}_{ij}|_{previous} + d\bar{\varepsilon}^{p(e)}_{ij}$;
   d. Repeat until $d\bar{\varepsilon}^{p(e)}_{ij}$ converges.
3. Evaluate the homogenized plastic strain increment $d\overline{\boldsymbol{\varepsilon}}^{p} = \sum_{e=1}^{N_e} c_{(e)}\boldsymbol{B}^{(e)}d\overline{\boldsymbol{\varepsilon}}^{p(e)}$;
4. Update $\overline{\boldsymbol{\varepsilon}}$ and $\overline{\boldsymbol{\varepsilon}}^{p}$ and calculate the homogenized stress $\overline{\boldsymbol{\sigma}} = \boldsymbol{C}^{*}\left(\overline{\boldsymbol{\varepsilon}} - \overline{\boldsymbol{\varepsilon}}^{p}\right)$.

3 RESULTS

3.1 Numerical Analysis

3.1.1 Problem Description

The elastoplastic analysis of periodically perforated metal sheets was carried out employing the concepts discussed in the previous sections to analyze the TFA's capabilities. The domain was discretized in several ways for the adoption of different types of elements. It should be noted that a similar analysis can be seen in Cavalcante and Pindera (2013). All analyzes were performed in a Matlab 2019a environment (The MathWorks Inc., 2019) with an Intel Core i7-7700HQ processor running at 3.80 GHz with 16 GBs of RAM.

The perforated metal sheet presents circular holes distributed in a hexagonal array with a volume fraction of 25%. Discretizations disposes the elements along the angular and radial directions: 18x3 (54 elements), 30x5 (150 elements) and 90x15 (1350 elements). Figure 2 shows the discretizations for quadrilateral elements.

The strain hardening of the aluminum matrix is described by a power-law hardening, which takes the form

$$\sigma_{eff} = \sigma_y + H_p\left(\varepsilon^{p}_{eff}\right)^{n} \tag{22}$$

where σ_y is the yield stress, H_p is the strain-hardening slope and n is the exponent of the power-law. Elastic and plastic parameters of the aluminum alloy employed in the perforated sheet studies and analyzed by Öchsner (2003): $E = 72.7\ MPa$, $\nu = 0.34, \sigma_y = 240\ MPa, H_p = 457.589\ MPa, n = 0.4218$.

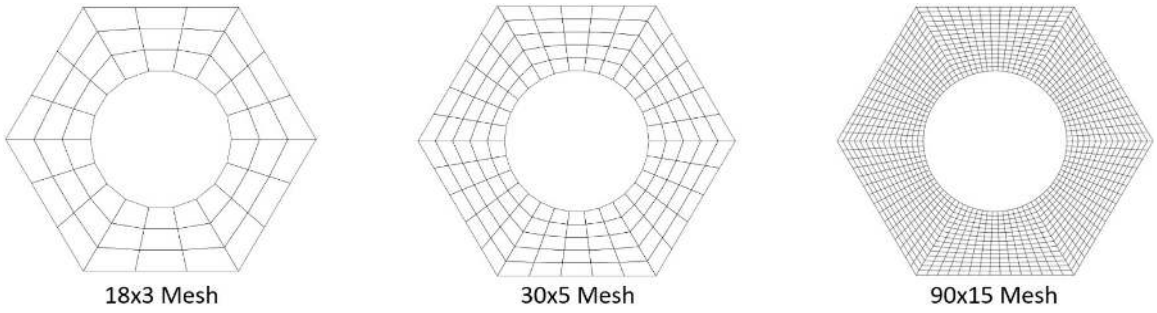


Figure 2: Discretizations of the unit cell.

Complementary to linear quadrilateral elements, a study is also made employing quadratic elements with the same meshes. In this case, the element can represent more complex strain fields, delivering better results than the linear element with less discretization. However, it is noteworthy that the number of nodes increases significantly. Table 1 shows a comparison between the number of nodes for each of the adopted meshes. A higher-order quadrilateral element with five-degree Lagrangian interpolation (or 36 nodes) is also employed. For instance, an 18x3 mesh has 54 elements and 1440 nodes, the same number of nodes of the 90x15 mesh with linear elements. With this higher-order element, it was possible to verify the influence of node density per element in the analyses.

Table 1: Number of elements and nodes per discretization.

	Discretizations		
	18x3	**30x5**	**90x15**
Elements	54	150	1350
Nodes (Linear Element)	72	180	1440
Nodes (Quadratic Element)	252	660	5580
Nodes (Fifth-Order Element)	1440	3900	34200

All models were subjected to periodic boundary conditions and macroscopic loadings to reflect uniaxial tension and pure shear scenarios. The load was applied in 30 equal increment steps until reaching homogeneous strains of 3%. Boundary conditions in the fluctuating displacement are established according to Figure 3 to avoid rigid body motions. The TFA results are compared with the classical Finite Element Analysis.

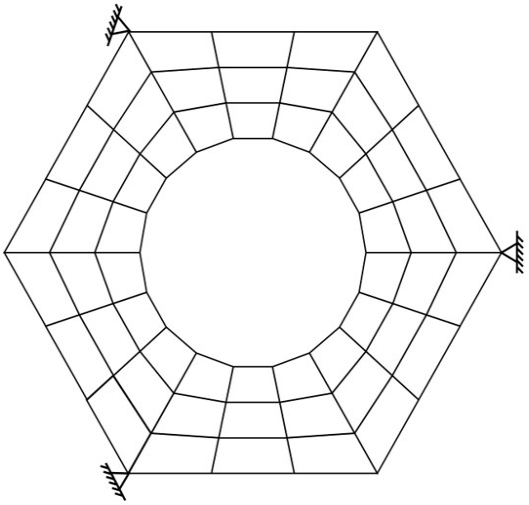


Figure 3: Displacement fluctuating restrictions.

The results are presented below, considering the scenarios of uniaxial tension and pure shear, Figure 4. The analyses were carried out as follows: comparing models employing the same finite element but with different mesh discretizations and models with the same number of nodes (the same number of degrees of freedom) but with different numbers of finite elements with distinguished orders. Thus, the objective was to highlight the influence of the mesh discretization

for the same type of finite element and the order of the employed finite element for the same number of nodes, i.e., the same number of degrees of freedom.

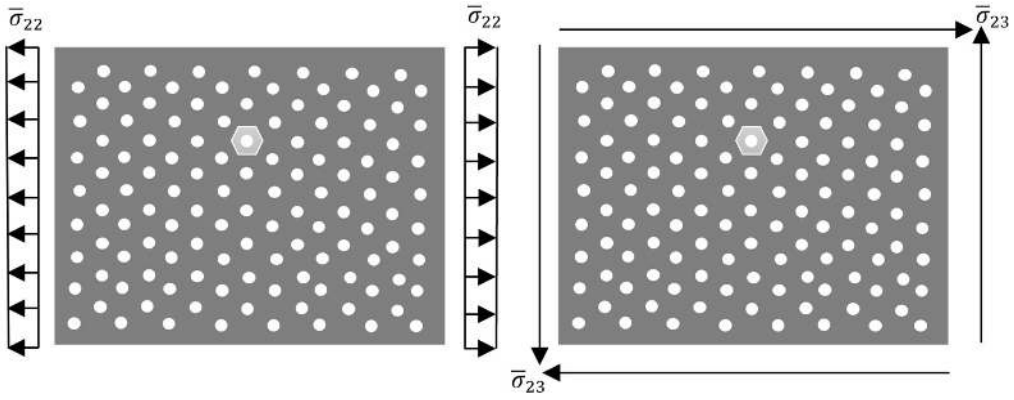


Figure 4: Uniaxial tension and pure shear macroscopic loadings.

3.1.2 Uniaxial Tension

Figure 5 shows the results of the models with all meshes using the linear, quadratic, and high-order elements. The TFA data is compared with classical FEA results.

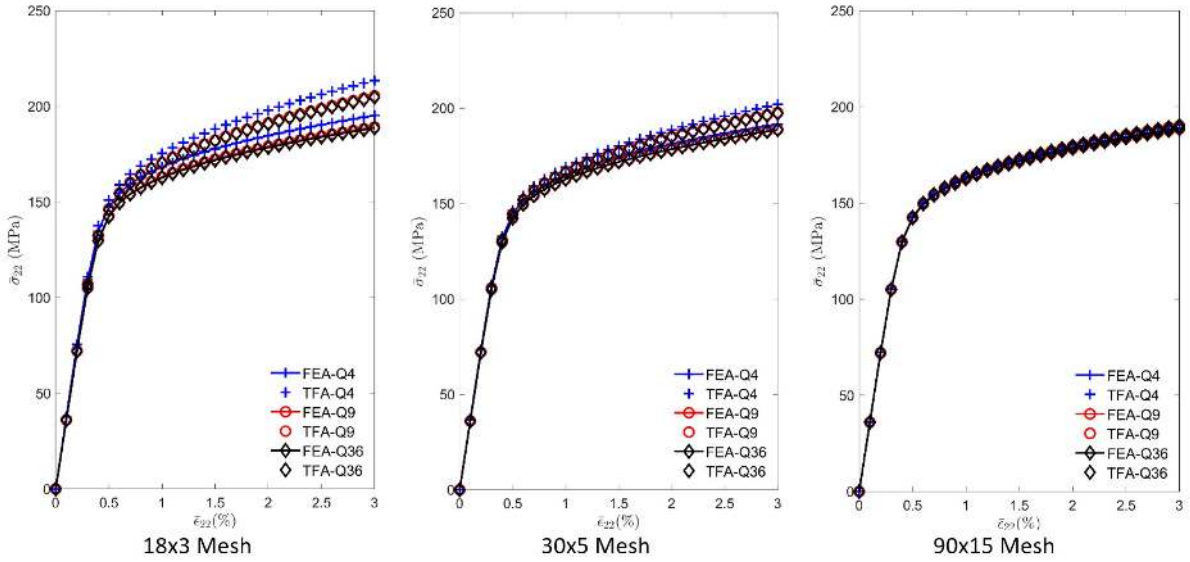


Figure 5: Macroscopic response for uniaxial tension employing FEA and TFA.

Table 2 shows the relative differences between the classical FEA and TFA for the same finite element and discretization (number of elements). Because TFA approximates stress/strain fields assuming uniform distribution per element, it was expected that TFA results would converge with FEA results for higher levels of discretization because it can capture the localized plastic strain field. The quadratic finite element presented similar results compared with the fifth-order finite element. Higher-order finite elements give a less stiff macroscopic response for TFA because they can more correctly capture the localized field when a uniform eigenstrain is imposed per element. For the coarsest meshes, the maximum relative difference was lower than 10% for the macroscopic strain of 3%, and for the most refined meshes, the relative differences were less than 1.5%.

The effective plastic strain and stress distributions are presented for the 90x15 meshes of linear, quadratic, and fifth-order finite elements (Figure 6, Figure 7, and Figure 8). These fields present uniform averaged distributions per element to compare the results obtained by classical FEA and TFA approaches more directly. For this level of discretization, the localized response obtained by TFA is as good as the localized response obtained by classical FEA for all the analyzed finite elements.

Table 2: Relative differences between FEA and TFA (uniaxial tension).

Uniaxial Tension						
Macroscopic Strain	**0.5%**	**1%**	**1.5%**	**2%**	**2.5%**	**3%**
Q4 18x3	2.50%	4.23%	5.78%	7.17%	8.34%	9.34%
Q4 30x5	1.11%	2.35%	3.26%	4.06%	4.77%	5.40%
Q4 90x15	0.16%	0.40%	0.61%	0.81%	0.98%	1.14%
Q9 18x3	2.57%	4.60%	5.80%	6.86%	7.79%	8.59%
Q9 30x5	1.42%	2.35%	3.10%	3.70%	4.22%	4.68%
Q9 90x15	0.17%	0.34%	0.49%	0.61%	0.73%	0.83%
Q36 18x3	2.58%	4.69%	5.89%	6.90%	7.78%	8.55%
Q36 30x5	1.44%	2.28%	3.02%	3.62%	4.13%	4.58%
Q36 90x15	0.18%	0.34%	0.48%	0.60%	0.72%	0.82%

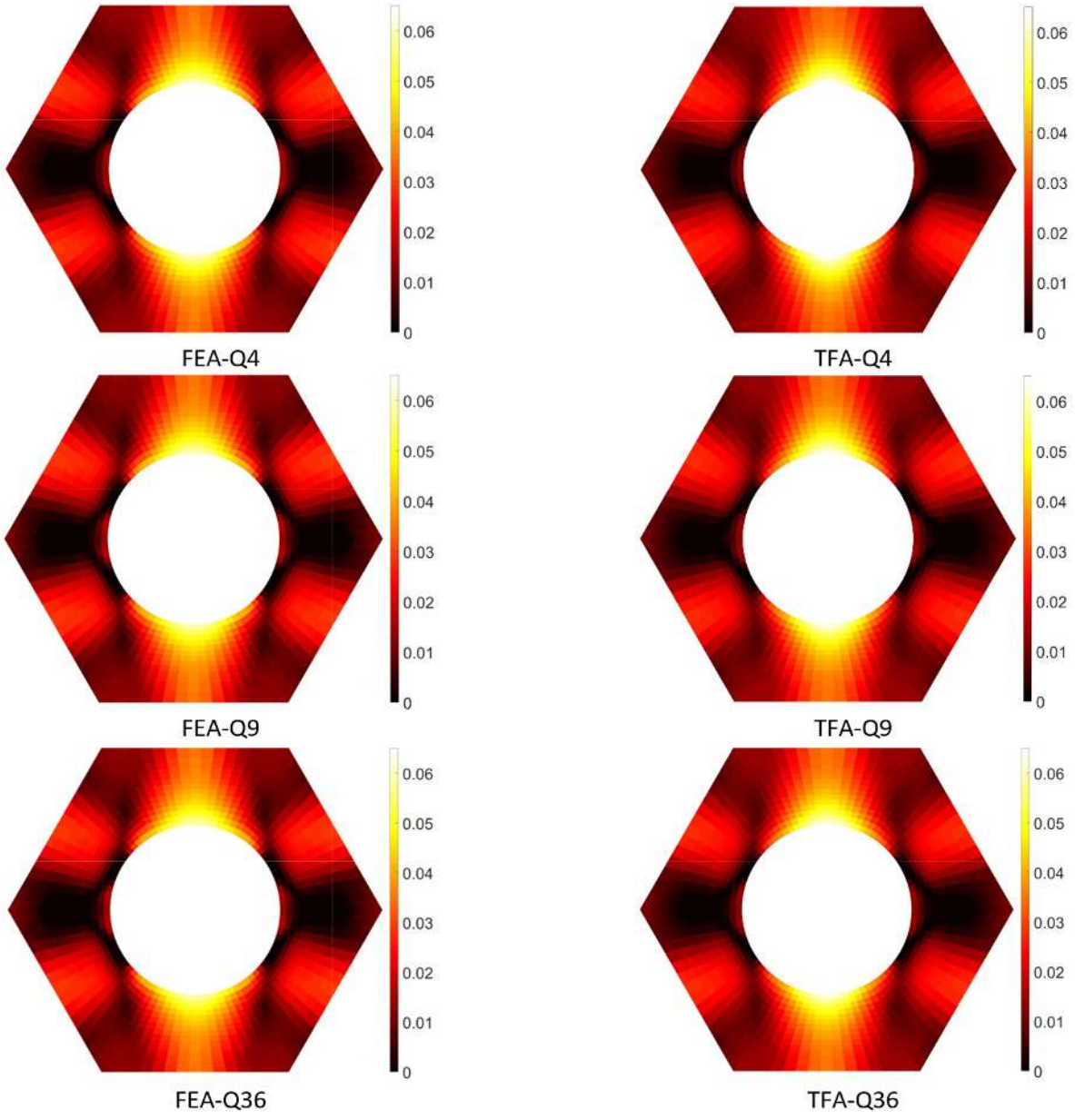


Figure 6: Effective plastic strain distributions for uniaxial tension.

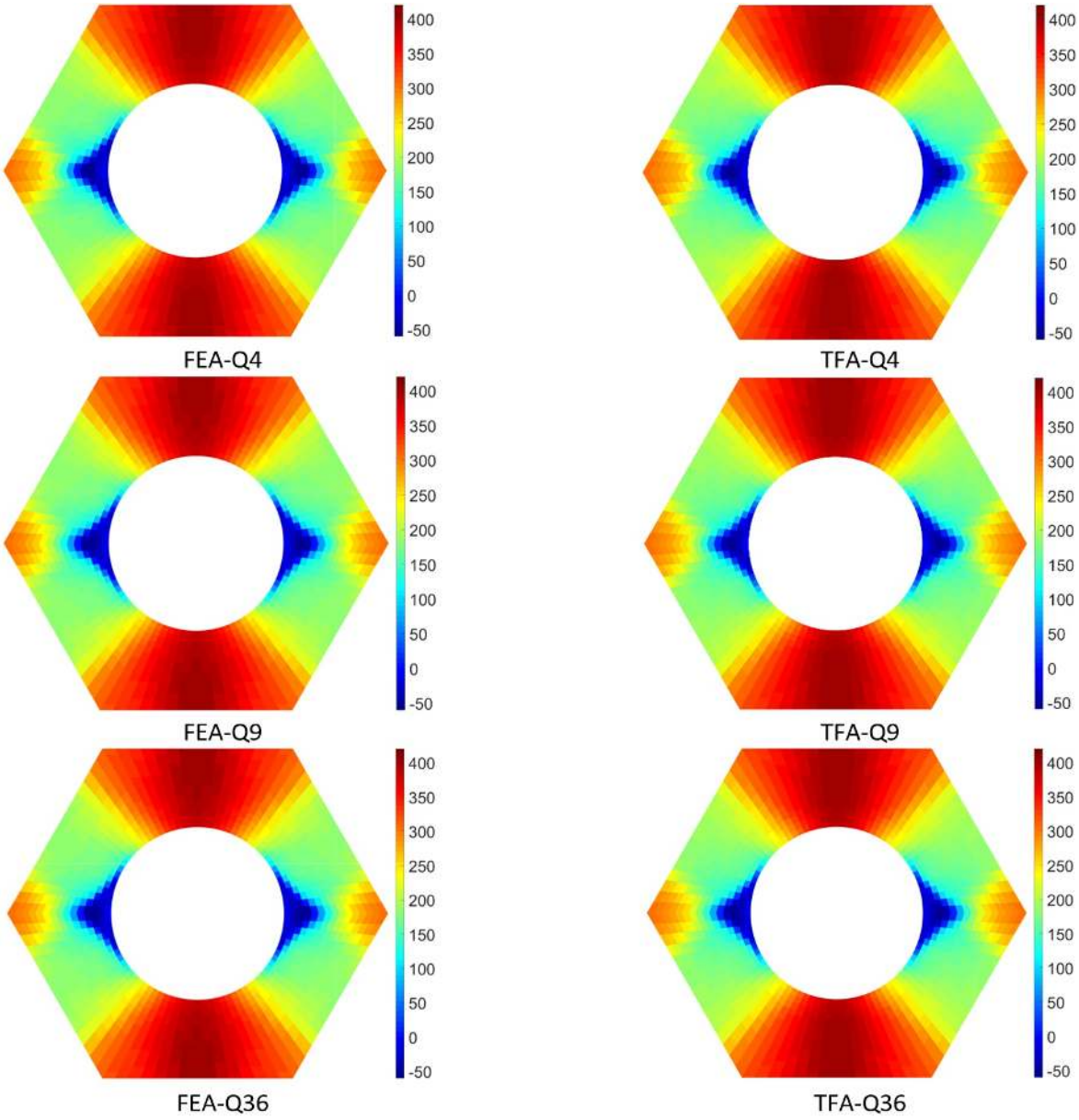


Figure 7: Horizontal normal stress distribution for uniaxial tension.

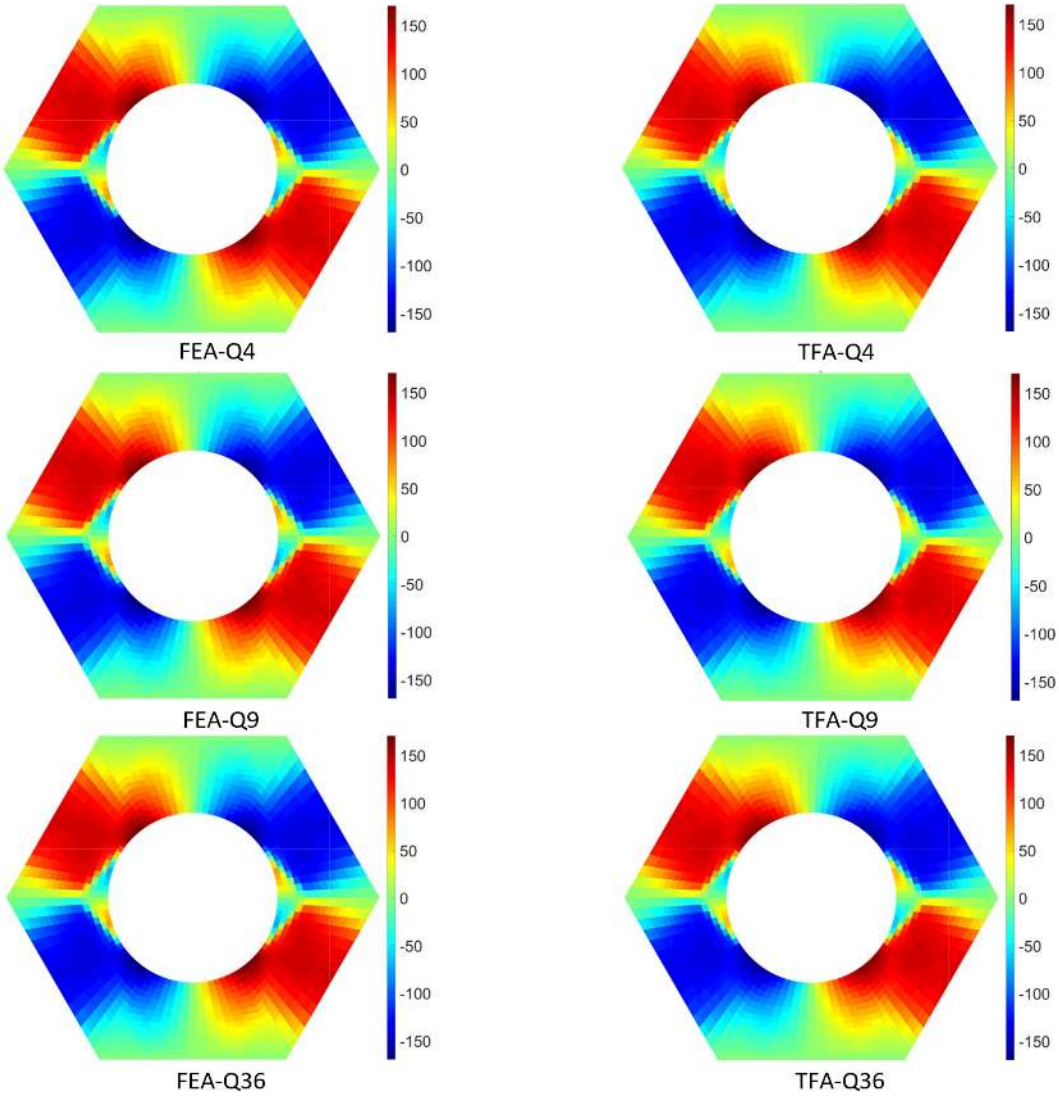


Figure 8: Shear stress distribution for uniaxial tension.

3.1.3 Pure Shear

Figure 9 and Table 3 show the results for a pure shear macroscopic loading. The macroscopic responses present similar trends to those presented in the case of macroscopic uniaxial tension. However, the macroscopic response is more affected by the discretization level and the order of the finite element for this case.

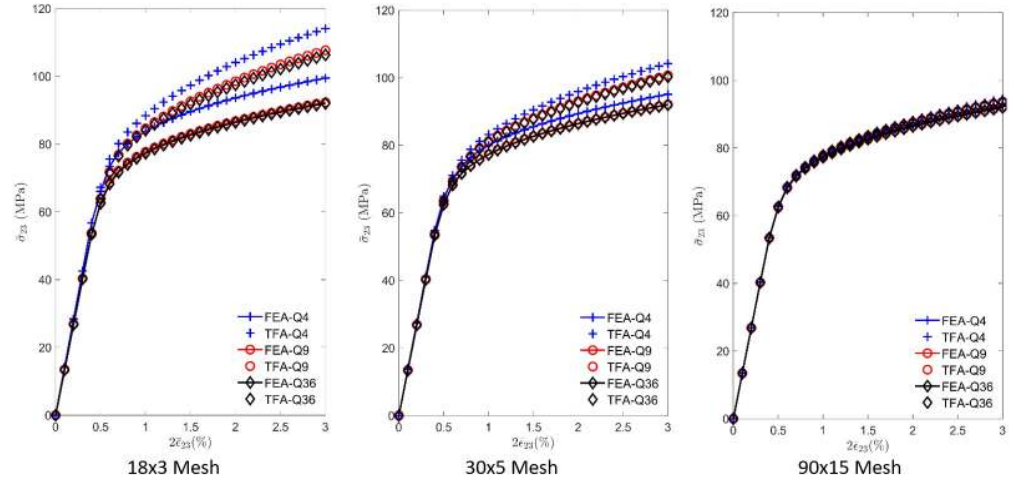


Figure 9: Macroscopic response for pure shear employing FEA and TFA.

Table 3: Relative differences between FEA and TFA (pure shear).

Pure Shear						
Macroscopic Strain	**0.5%**	**1%**	**1.5%**	**2%**	**2.5%**	**3%**
Q4 18x3	1.81%	5.56%	8.69%	11.14%	13.08%	14.66%
Q4 30x5	1.02%	3.98%	5.77%	7.31%	8.52%	9.53%
Q4 90x15	0.15%	0.77%	1.29%	1.70%	2.05%	2.35%
Q9 18x3	1.89%	8.90%	11.58%	13.59%	15.29%	16.60%
Q9 30x5	1.72%	4.96%	6.41%	7.59%	8.55%	9.38%
Q9 90x15	0.19%	0.73%	1.11%	1.40%	1.64%	1.85%
Q36 18x3	2.03%	8.87%	11.15%	12.86%	14.29%	15.59%
Q36 30x5	1.72%	4.84%	6.21%	7.30%	8.20%	8.98%
Q36 90x15	0.19%	0.72%	1.08%	1.37%	1.60%	1.81%

As seen in uniaxial tension, an increased number of elements results in lower differences among the approaches. In this case, the maximum relative difference for the most refined meshes is lower than 3%, while for the coarsest meshes, the relative difference peaked at almost 17%. These results corroborate for TFA to be employed with a higher level of discretization and with higher-order finite elements.

For the macroscopic pure shear, effective plastic strain and stress fields are shown for 90x15 meshes of linear, quadratic, and fifth-order finite elements (Figure 10, Figure 11, and Figure 12). These fields present uniform averaged distributions per element to compare the results obtained by classical FEA and TFA approaches more directly. Once again, for this level of discretization, the localized response obtained by TFA is as good as the localized response obtained by classical FEA for all the analyzed finite elements.

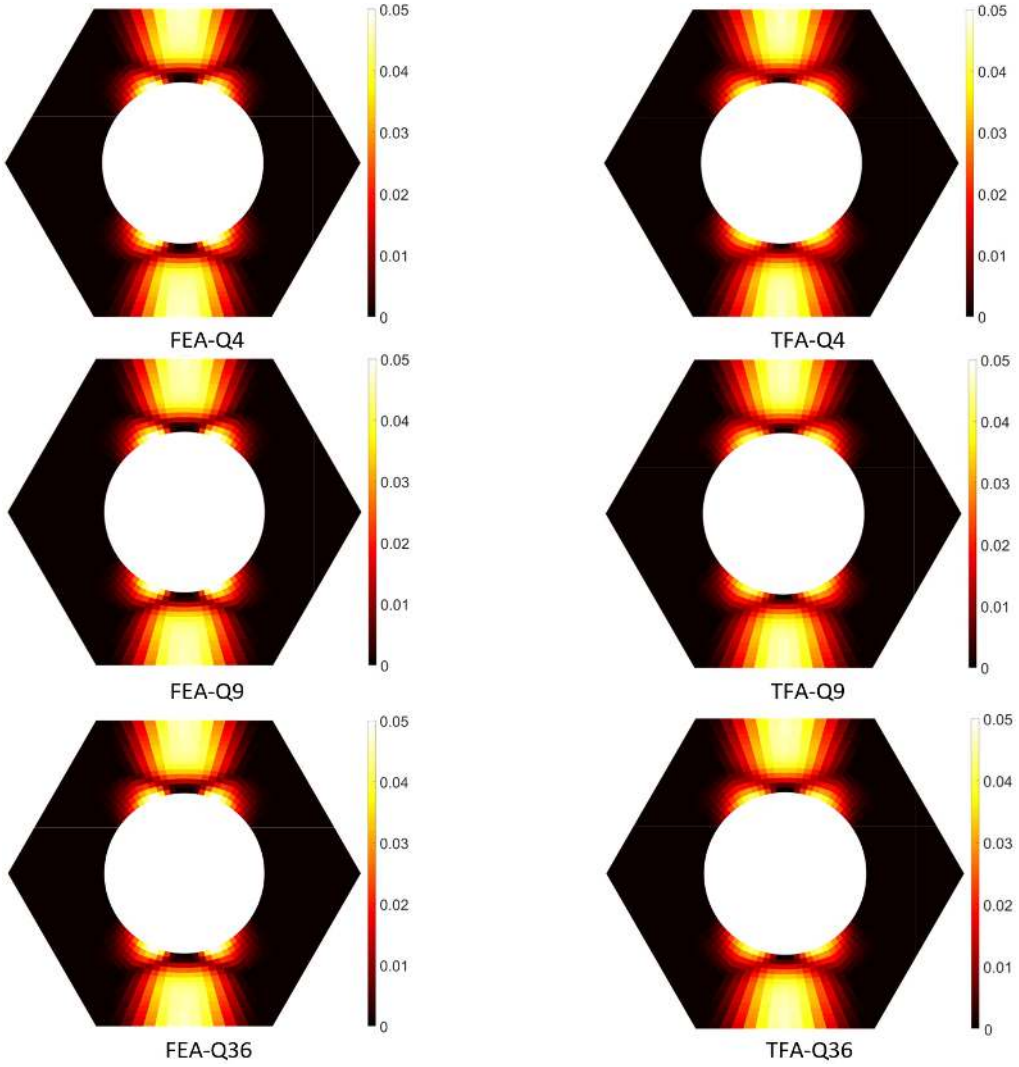


Figure 10: Effective plastic strain distributions for pure shear.

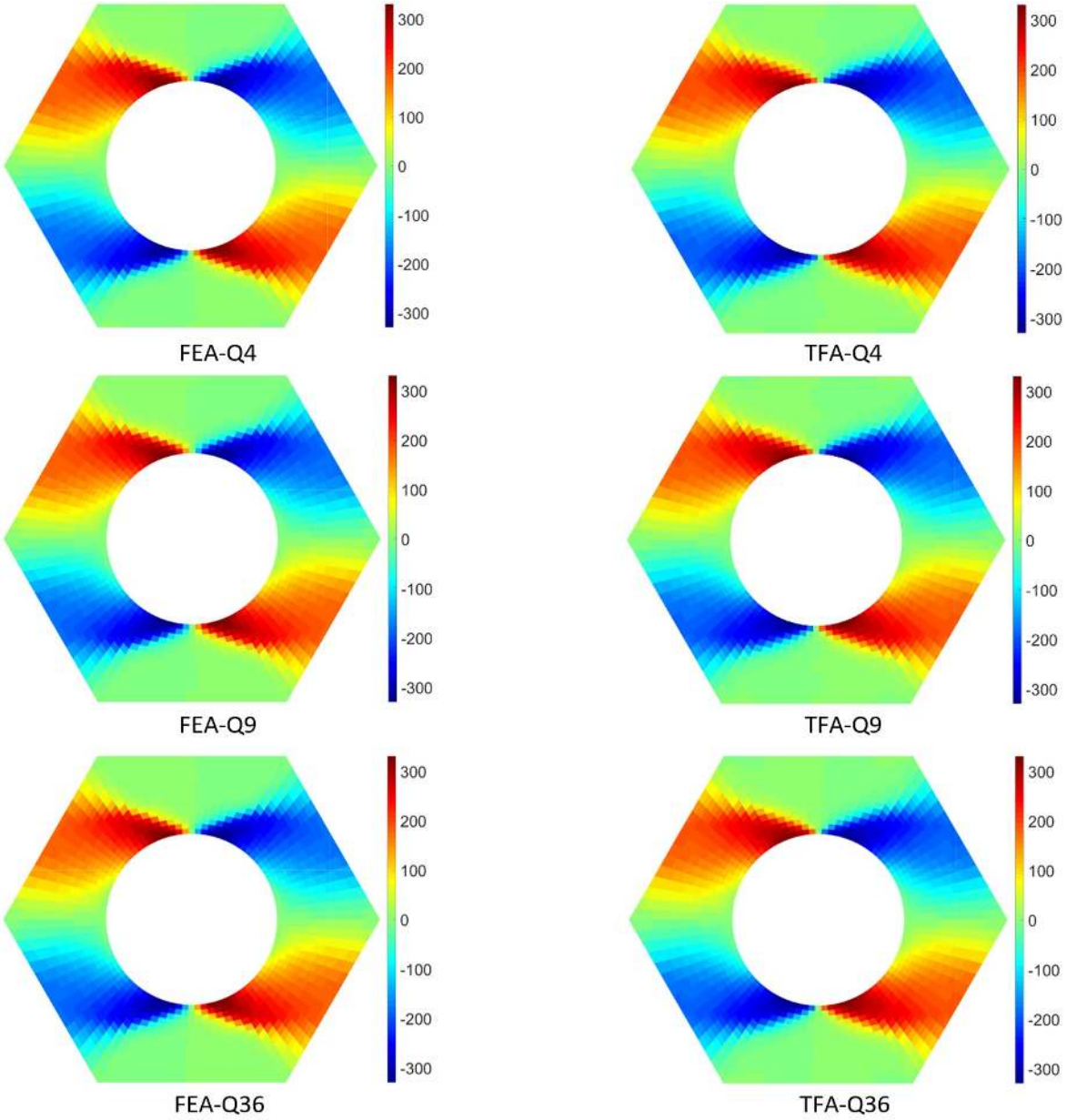


Figure 11: Horizontal normal stress distribution for pure shear.

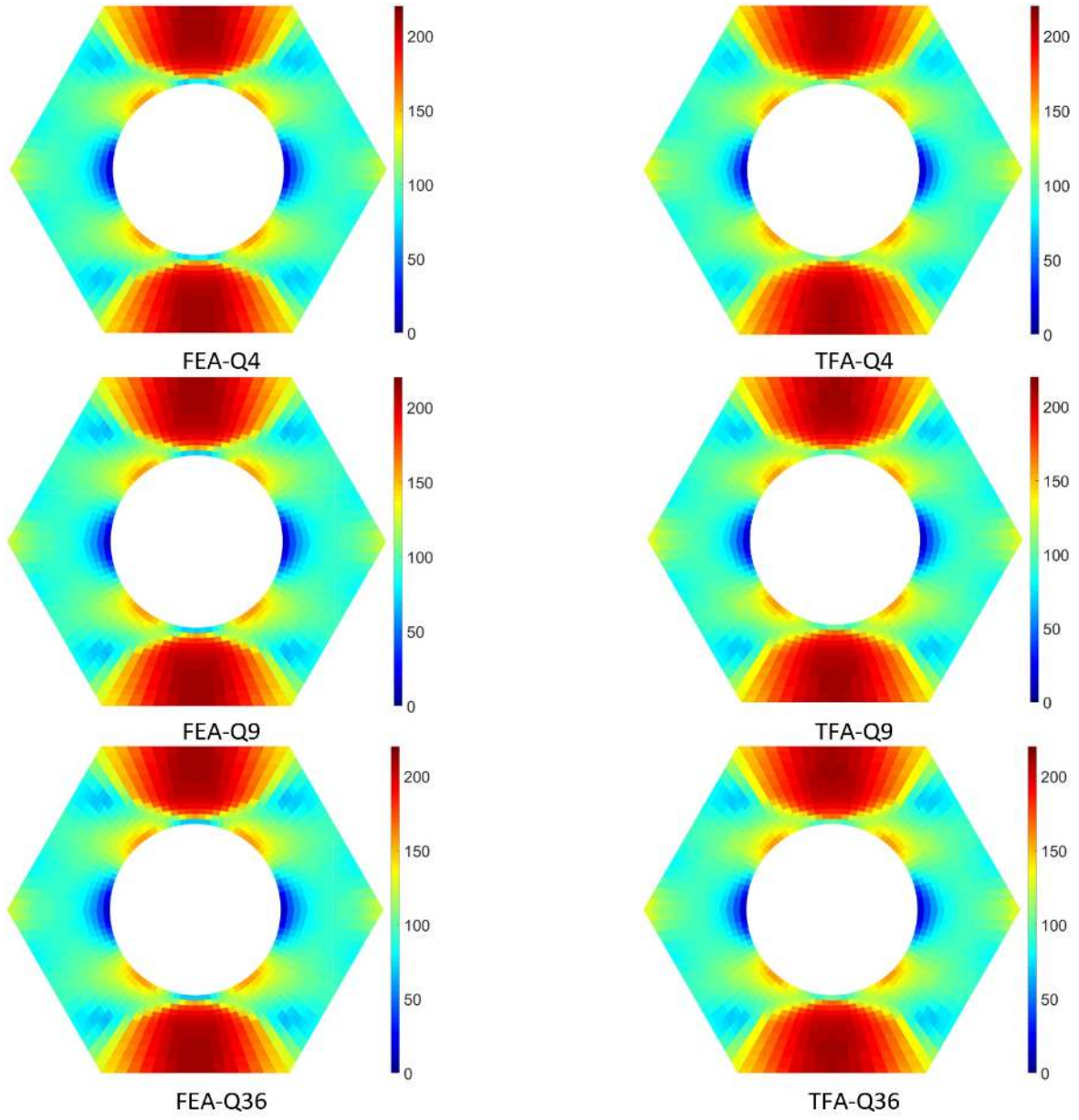


Figure 12: Shear stress distribution for pure shear.

3.2 Experimental Validation

The coupling TFA-FEM is also analyzed employing an experiment found in Öchsner (2003) for elastic-plastic analysis of perforated metal sheets under uniaxial tension, as shown in Figure 13. Experimental tests employed void fractions of 19% and 28%. Three discretization levels were adopted: the coarsest meshes have 1680 nodes, and the most refined meshes have 3720 nodes. Elements of first, second and fifth order were organized into these meshes. Table 4 shows the number of elements and nodes for each discretization level. All meshes for 28% void fraction are shown with the element's distribution in Figure 14.

Figure 15 shows the results for the two void fractions and all discretizations. As can be seen, finer discretization leads to results closer to the experimental data. Also, the macroscopic response obtained by the numerical simulations is stiffer than the experimental values; the board's effect can explain this once a traction-free condition can be observed in the experimental test.

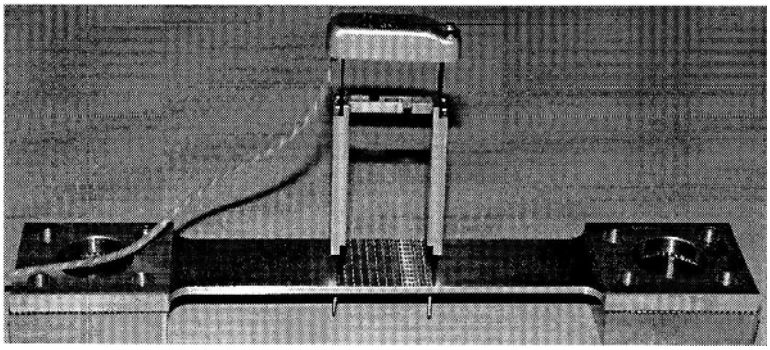


Figure 13: Öschner experiment.

Table 4: Discretization levels and domain subdivisions.

	Coarse Mesh (C)	Intermediate Mesh (I)	Fine Mesh (F)
Number of Nodes	440	1680	3720
Linear Elements	400	1600	3600
Quadratic Elements	100	400	900
5th Order Elements	16	64	144

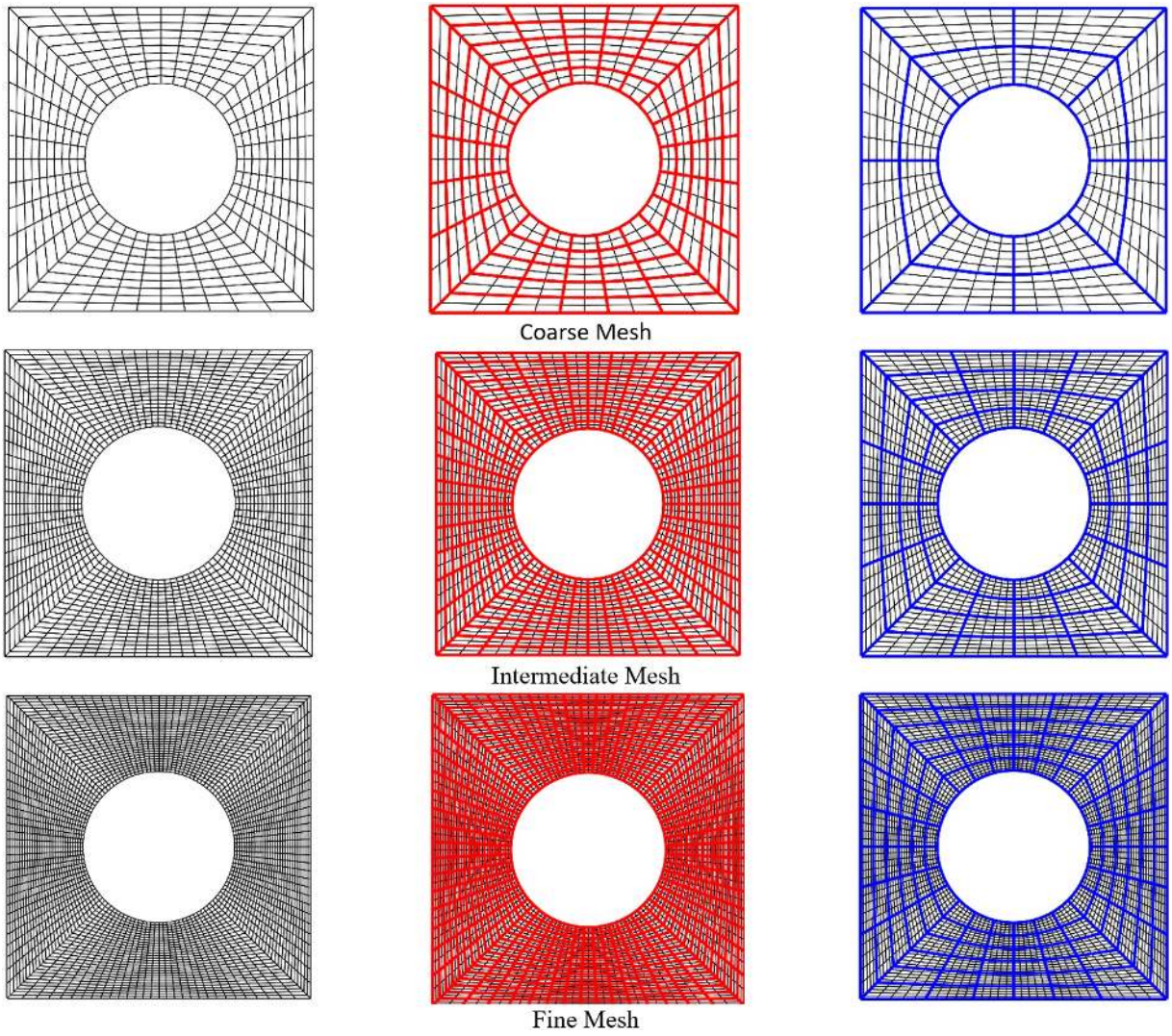


Figure 14: Meshes for the 28% void fraction and distribution of linear (black), quadratic (red) and fifth-order (blue) finite elements.

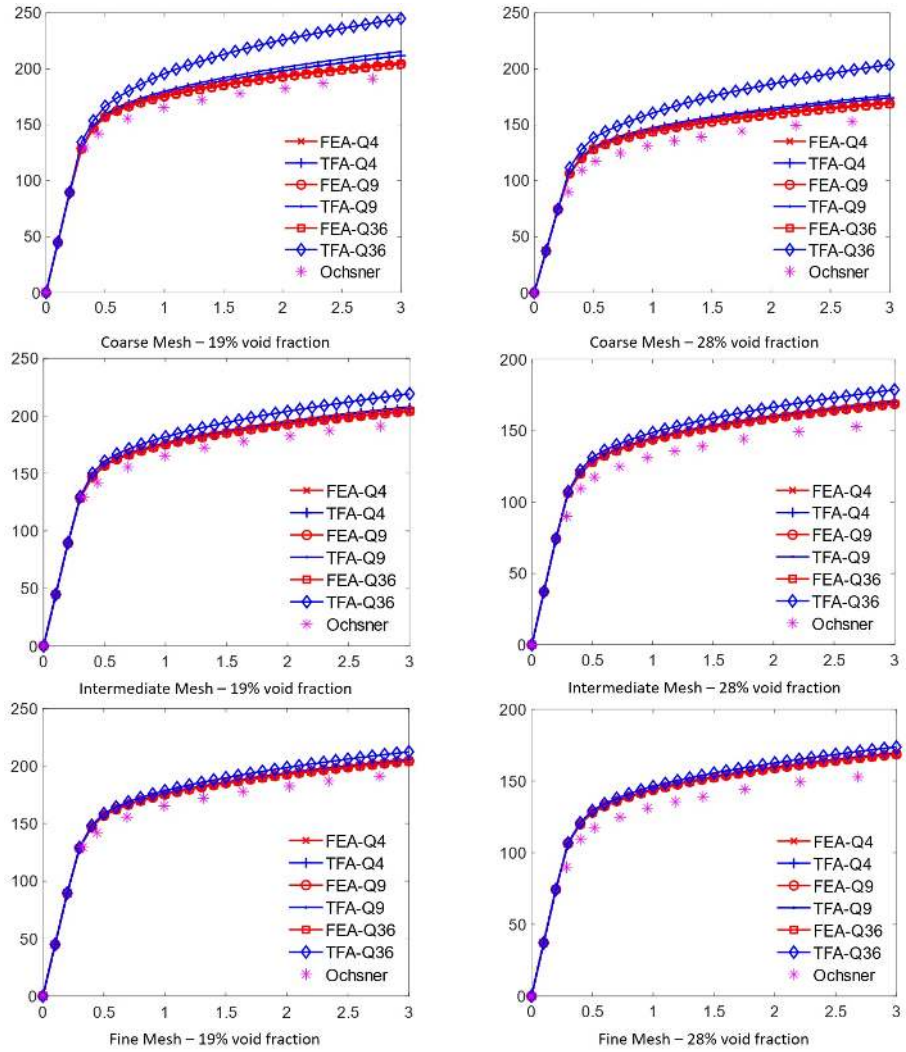


Figure 15: Numerical and experimental results for 19% and 28% void fractions [$\overline{\sigma}_{22}(MPa)\ x\ \overline{\varepsilon}_{22}(\%)$].

Table 5 and Table 6 present relative differences between the numerical and experimental results for the fine meshes. As expected, FEA and TFA resulted in stiffer responses due to the board's effect caused by the traction-free condition in the experimental test. The difference between macroscopic stresses increased alongside macroscopic strain evolution, culminating in a maximum divergence of 4% between TFA and FEA using the fifth-order element for the 19% void fraction. The relative differences between FEA and TFA for meshes using linear and quadratic elements were less than 1%.

As results show, there are situations where the coupling of Transformation Field Analysis with Finite Element Method can present accurate data compared with classical FEA. It is also essential to assess the computational cost regarding this analysis to understand TFA's potential as a viable alternative to classical FEA.

Table 5: Relative diferrences between the numerical and experimental results for void fraction of 19%.

Macroscopic Strain (%)	FEA			TFA			Difference		
	Q4	Q9	Q36	Q4	Q9	Q36	Q4	Q9	Q36
0.4	3.64%	3.57%	3.56%	3.70%	3.77%	4.59%	0.06%	0.19%	1.03%
0.7	7.01%	6.95%	6.94%	7.12%	7.23%	8.51%	0.10%	0.29%	1.57%
1	6.06%	5.99%	5.98%	6.23%	6.38%	7.98%	0.17%	0.40%	1.99%
1.3	5.55%	5.47%	5.47%	5.79%	5.97%	7.87%	0.24%	0.49%	2.40%
1.6	5.08%	5.00%	5.00%	5.39%	5.58%	7.81%	0.31%	0.58%	2.81%
2	5.65%	5.57%	5.57%	6.05%	6.26%	8.88%	0.39%	0.69%	3.32%
2.3	5.12%	5.03%	5.03%	5.57%	5.80%	8.63%	0.45%	0.77%	3.60%
2.8	5.88%	5.79%	5.79%	6.42%	6.68%	9.85%	0.55%	0.89%	4.06%

Table 6: Relative diferrences between the numerical and experimental results for void fraction of 28%.

Macroscopic Strain (%)	FEA			TFA			Difference		
	Q4	Q9	Q36	Q4	Q9	Q36	Q4	Q9	Q36
0.4	9.69%	9.60%	9.58%	9.73%	9.81%	10.56%	0.04%	0.20%	0.98%
0.5	9.16%	9.07%	9.06%	9.21%	9.29%	10.28%	0.05%	0.23%	1.22%
0.7	9.08%	8.99%	8.98%	9.16%	9.29%	10.57%	0.08%	0.30%	1.58%
1	9.74%	9.65%	9.65%	9.88%	10.02%	11.52%	0.13%	0.37%	1.87%
1.2	8.92%	8.83%	8.82%	9.08%	9.24%	10.81%	0.16%	0.41%	1.99%
1.4	8.62%	8.53%	8.52%	8.81%	8.97%	10.66%	0.19%	0.45%	2.14%
1.8	8.59%	8.49%	8.49%	8.83%	9.01%	10.93%	0.25%	0.51%	2.44%
2.2	7.93%	7.83%	7.83%	8.23%	8.41%	10.54%	0.30%	0.58%	2.71%
2.7	8.74%	8.64%	8.64%	9.11%	9.30%	11.71%	0.38%	0.66%	3.08%

3.4 Performance Analysis

The computational cost analysis is crucial due to the cost-benefit aspect regarding the increase of domain discretization and the adoption of higher-order finite elements. It is essential not only to evaluate the accuracy of both methods (as presented in the previous section) but to appraise the computational time of both approaches. It is important to remark that all computational effort measured considers only the elastoplastic analysis, i.e., the computational cost involving the calculation of the strain concentration and influence tensors for TFA was not computed. However, once evaluating these tensors, any macroscopic loading can be imposed on the model, generating failure surfaces, for instance.

As said before, the application of TFA coupled with FEM changes the formulation used to evaluate the macroscopic response of periodic media. Classical FEA assembles and solves a linear equation system to find displacement and, therefore, strain and stress – this step is considered the main bottleneck of the method. TFA finds strain field by summation of a multiplication of the pre-calculated tensors with the local uniform strain of each finite element of the discretized analysis domain. Both operations can become cumbersome depending on the model's size: TFA's advantage can become a problem if domain discretization is too high because, for N elements, there are N^2 influence tensors. In the sequence, classical FEA computational time is compared with sequential and parallel TFA. The parallelization technique is only applied in the summation step and shows the TFA's potential.

All analyzes were performed in a Matlab 2019a environment (The MathWorks Inc., 2019) with an Intel Core i7-7700HQ processor running at 3.80 GHz with 16 GBs of RAM. Figure 16 shows computational time spent in all simulations of the Ochsner results, except TFA's processing time for the intermediate and fine meshes using linear elements because it was too high and exceeded the plots. On the other hand, Table 7 and Table 8 show all processing time measured.

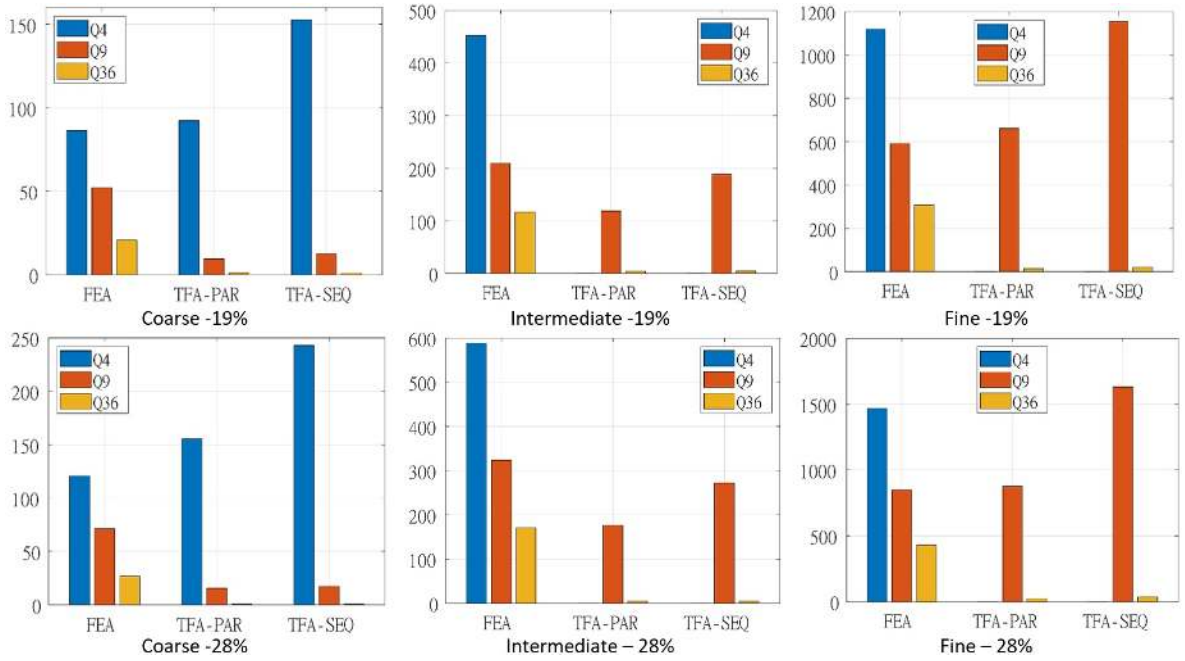


Figure 16: Processing times of elastoplastic analysis of the Ochsner experiments (seconds).

Table 7: Processing time in seconds for FEA and TFA (void fraction of 19%).

	Coarse Mesh			Intermediate Mesh			Fine Mesh		
	FEA	**TFA SEQ**	**TFA PAR**	**FEA**	**TFA SEQ**	**TFA PAR**	**FEA**	**TFA SEQ**	**TFA PAR**
Q4	86.40	153.00	92.00	452.40	3116.00	1906.00	1119.20	18124.00	25324.00
Q9	52.06	12.50	9.56	209.07	188.50	118.68	592.34	1154.50	661.75
Q36	21.11	0.69	0.79	133.86	4.64	4.20	334.67	20.05	14.69

Table 8: Processing time in seconds for FEA and TFA (void fraction of 28%).

	Coarse Mesh			Intermediate Mesh			Fine Mesh		
	FEA	**TFA SEQ**	**TFA PAR**	**FEA**	**TFA SEQ**	**TFA PAR**	**FEA**	**TFA SEQ**	**TFA PAR**
Q4	120.60	243.000	155.000	588.00	4512.000	2854.000	1467.10	24536.000	41281.000
Q9	71.35	17.400	15.838	323.47	272.500	176.808	848.31	1632.700	874.656
Q36	26.02	0.773	0.696	162.12	4.832	4.699	459.14	33.185	24.309

TFA's computational cost increases as discretization increases, which can be seen in the results for both void fractions. However, in the case of linear elements, considering the fine mesh, the communication between cores becomes so cumbersome that using sequential TFA presents a lower computational cost relative to the parallel TFA. This problem can be addressed by increasing the number of cores or employing more powerful CPUs or GPU-based parallel programming.

In the analyses employing the quadratic finite element, both sequential and parallel TFA presented lower computational costs than the FEA, considering the coarse and intermediate meshes. For the fine mesh, the parallel TFA presented slightly higher times than those observed in the classical FEA. The parallel TFA performed better than the sequential TFA for all meshes.

In terms of computational cost, the best results employing TFA were obtained by higher-order elements, as observed for the fifth-order finite element. Delivering a maximum of 4% difference relative to the FEA, sequential TFA obtained results using only 7% of the time spent with classical FEA. Using parallel TFA, this time drops to 5%. However, it is necessary to refine the mesh to obtain more accurate results without substantially increasing the computational cost.

4 CONCLUSIONS

The association between the discretization of the mesh and the stiffness of the FEA result is well known. This relation is associated with the element capacity to represent the local deformation: the deformation representation is simplified by decreasing the element size, demanding less from the finite element to represent the local response.

The coupling of TFA with higher-order finite elements improves the concordance with the classical FEA results. However, the employment of higher-order finite elements must be integrated with a suitable discretization of the mesh. The mesh refinement is more critical in obtaining better results with TFA than the application of higher-order finite elements. Thus, capturing the localized plastic strains by a refined mesh is more critical than the tendency to obtain stiffer results due to the limitation of the finite element to represent the local response when a lower-order finite element is employed.

Subsequently, numerical results were compared to experimental data obtained in the literature. This investigation consists of perforated metal sheets with two void fractions subjected to uniaxial tension and pure shear macroscopic loadings. Although the simulations presented stiffer responses for all the adopted meshes due to the board's effect caused by the traction-free condition in the experimental test, numerical results were reasonably close to experimental values. The worst results obtained from this investigation showed a relative difference of 4% in the macroscopic stress between classical FEA and TFA.

The last analysis assessed the computational costs of FEA and TFA approaches. The TFA adopts the simplification of uniform fields in the elements of the discretized analysis domain. The TFA was faster for the coarse and intermediate meshes when compared to the respective classical FEA, independently of the adopted finite element. Only the higher-order finite element presented a smaller computational cost for the fine mesh when compared to the respective classical FEA. Nevertheless, more refined meshes performed better, and good levels of accuracy were achieved, culminating with a maximum of 4% relative difference for the higher-order finite element, but obtaining results for the sequential TFA with only 7% of the time spent in classical FEA. This time drops to 5% for the parallel TFA. Also, the parallel TFA employing quadratic finite elements performed better or presented similar processing times when compared to the respective classical FEA.

The advantages of the TFA for elastoplastic analysis of periodically perforated metal sheets are highlighted. In all cases, the processing time to generate the elements' strain concentration and influence tensors was not considered. After obtaining these tensors, any macroscopic loadings can be imposed, including those necessary to generate the failure surfaces. Thus, the TFA can be well employed in cases where the discretization of the mesh and the element's order can produce good results with less computational cost when compared to the classical FEA.

Author Contributions: Conceptualization, MAA Cavalcante; Investigation, CAF Várady Filho; Methodology, CAF Várady Filho and MAA Cavalcante; Supervision, MAA Cavalcante; Validation, CAF Várady Filho; Writing – original draft, CAF Várady Filho; Writing – review & editing, CAF Várady Filho and MAA Cavalcante.

Editor: Marcílio Alves.

References

Addessi, D., Sacco, E., Paolone, A. (2010). Cosserat model for periodic masonry deduced by nonlinear homogenization. Eur. J. Mech. A/Solids 29: 4.

Alaimo, G., Auricchio, F., Marfia, S., Sacco, E. (2019). Optimization clustering technique for PieceWise Uniform Transformation Field Analysis homogenization of viscoplastic composites. Comput. Mech. 64: 6, 1495–1516.

Benveniste, Y., Dvorak, G. J. (1990). On a Correspondence Between Mechanical and Thermal Effects in Two-Phase Composites. Micromechanics and Inhomogeneity, 65–81.

Benveniste, Y., Dvorak, G. J. (1992). Some Remarks on a Class of Uniform Fields in Fibrous Composites. J. Appl. Mech. 59: 4, 1030–1032.

Cavalcante, M. A. A., Pindera, M.-J. (2013). Finite-volume enabled transformation field analysis of periodic materials. Int. J. Mech. Mater. Des. 9: 2, 153–179.

Cavalcante, M. A. A., Pindera, M.-J. (2016). Generalized FVDAM theory for elastic–plastic periodic materials. Int. J. Plast. 77: 90–117.

Covezzi, F., Miranda, S. de, Fritzen, F., Marfia, S., Sacco, E. (2018). Comparison of reduced order homogenization techniques: pRBMOR, NUTFA and MxTFA. Meccanica 53: 6, 1291–1312.

Covezzi, F., Miranda, S. de, Marfia, S., Sacco, E. (2017). Homogenization of elasticviscoplastic composites by the Mixed TFA. Comput. Methods Appl. Mech. Eng. 318: 701-723.

Drago, A. S., Pindera, M.-J. (2007). Micro-macromechanical analysis of heterogeneous materials: Macroscopically homogeneous vs periodic microstructures. Compos. Sci. Technol. 67: 6, 1243–1263.

Drago, A. S., Pindera, M.-J. (2008). A Locally Exact Homogenization Theory for Periodic Microstructures with Isotropic Phases. J. Appl. Mech. 75: 5.

Dvorak, G. J. (1986). Thermal Expansion of Elastic-Plastic Composite Materials. J. Appl. Mech. 53: 4, 737–743.

Dvorak, G. J. (1990). On uniform fields in heterogeneous media. Proc. R. Soc. London A Math. Phys. Eng. Sci. 431, 89–110.

Dvorak, G. J., Bahei-El-Din, Y. A., Wafa, A. M. (1994). The modeling of inelastic composite materials with the transformation field analysis. Model. Simul. Mater. Sci. Eng. 2, 571–586.

Dvorak, G. J., Benveniste, Y. (1992). On transformation strains and uniform fields in multiphase elastic media. Proc. R. Soc. London. Ser. A Math. Phys. Sci. 437, 291–310.

Fritzen, F., Leuschner, M. (2013). Reduced basis hybrid computational homogenization based on a mixed incremental formulation. Comput. Methods Appl. Mech. Eng. 260: 143–154.

Fritzen, F., Marfia, S., Sepe, V. (2015). Reduced order modeling in nonlinear homogenization: A comparative study. Comput. Struct. 157, 114–131.

Hill, R. (1963). Elastic properties of reinforced solids: Some theoretical principles. J. Mech. Phys. Solids 11: 5, 357–372.

MathWorks Inc. (2019) Matlab 2019a.

Mendelson, A. (1968). Plasticity, Theory and Application. First edition, Robert E. Krieger Publishing Company, USA.

Michel, J. C., Suquet, P. (2003). Nonuniform transformation field analysis. Int. J. Solids Struct. 40: 25.

Michel, J. C., Suquet, P. (2004). Computational analysis of nonlinear composite structures using the nonuniform transformation field analysis. Comput. Methods Appl. Mech. Eng. 193: 48.

OCHSNER, A. (2003). Experimentelle und numerische Untersuchung des elastoplastischen Verhaltens zellularer Modellwerkstoffe. Fortschritt-Berichte VDI 18: 282.

Paley, M., Aboudi, J. (1992). Micromechanical analysis of composites by the generalized cells model. Mech. Mater. 14: 2, 127–139.

Pindera, M.-J., Bednarcyk, B. A. (1999). An efficient implementation of the generalized method of cells for unidirectional, multi-phased composites with complex microstructures. Compos. Part B Eng. 30: 1, 87–105.

Roussette, S., Michel, J. C., Suquet, P. (2009). Nonuniform transformation field analysis of elastic-viscoplastic composites. Compos. Sci. Technol. 69: 1, 22–27.

Sepe, V., Marfia, S., Sacco, E. (2013). A nonuniform TFA homogenization technique based on piecewise interpolation functions of the inelastic field. Int. J. Solids Struct. 50: 5, 725–742.

Wang, G., Pindera, M. J. (2016). Locally-exact homogenization theory for transversely isotropic unidirectional composites. Mech. Res. Commun. 78, 2–14.

Yang, Z., Liu, Y., Sun, Y., Jing, Y., Qiang M. (2020). A novel second-order reduced homogenization approach for nonlinear thermo-mechanical problems of axisymmetric structures with periodic micro-configurations. Comput. Methods Appl. Mech. Eng. 368, 113-126.